Finite element analysis of square FRP-concrete-steel columns under eccentric compression

Amin Izadi
University of Wollongong, ai754@uowmail.edu.au

Lip H. Teh
University of Wollongong, lteh@uow.edu.au

Aziz Ahmed
University of Wollongong, aziza@uow.edu.au

Maria Anna Polak
University of Waterloo

Finite element analysis of square FRP-concrete-steel columns under eccentric compression

Abstract

This paper presents the development of a finite element (FE) methodology for investigating the behavior of the FRP, concrete and steel components of a square FRP-concrete-steel composite (FCSC) columns with a rotated square inner steel tube. The FE models are developed in ABAQUS using the authors' recently refined Concrete Damage Plasticity Model (CDPM) in conjunction with the FRP damage criteria available in the literature. The developed FE methodology is verified against the authors' experimental test results involving columns with normal and rotated square inner steel tubes under eccentric loading, and the FE analysis results are used to explain the column behavior and failure. The most vulnerable region of the concrete column was confirmed to be the corner, where the sandwiched concrete was the most confined in the diagonal direction of the cross-section. Coupled with the findings that the GFRP hoop strain at the corner was typically less than one third of the rupture strain when the column suddenly failed, and that the corner hoop strains at column failure varied by up to 100% between specimens even though the same GFRP material was used, it indicates the possibility that rather than the FRP rupture leading to concrete failure, the concrete failure precipitated the "premature" FRP rupture. Rotating the square inner steel tube reduced the vulnerability of the sandwiched concrete in the non-uniformly confined and compressed corner regions, leading to higher resistance and/or greater ductility of the FCSC column. The beneficial effects diminished with increasing eccentricity, partly due to yielding of the rotated inner steel tube on the tensile side as the material was further from the neutral axis of bending.

Disciplines

Engineering | Science and Technology Studies

Publication Details
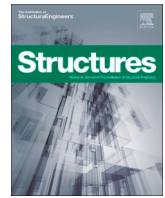
Finite element analysis of square FRP-concrete-steel columns under eccentric compression

Amin Izadi [a], Lip H. Teh [a,*], Aziz Ahmed [a], Maria Anna Polak [b]

[a] School of Civil, Mining, Environmental and Architectural Engineering, University of Wollongong, Wollongong, Australia
[b] Department of Civil and Environmental Engineering, University of Waterloo, Waterloo, ON, Canada

ARTICLE INFO

ABSTRACT

This paper presents the development of a finite element (FE) methodology for investigating the behavior of the FRP, concrete and steel components of a square FRP-concrete-steel composite (FCSC) columns with a rotated square inner steel tube. The FE models are developed in ABAQUS using the authors' recently refined Concrete Damage Plasticity Model (CDPM) in conjunction with the FRP damage criteria available in the literature. The developed FE methodology is verified against the authors' experimental test results involving columns with normal and rotated square inner steel tubes under eccentric loading, and the FE analysis results are used to explain the column behavior and failure. The most vulnerable region of the concrete column was confirmed to be the corner, where the sandwiched concrete was the most confined in the diagonal direction of the cross-section. Coupled with the findings that the GFRP hoop strain at the corner was typically less than one third of the rupture strain when the column suddenly failed, and that the corner hoop strains at column failure varied by up to 100% between specimens even though the same GFRP material was used, it indicates the possibility that rather than the FRP rupture leading to concrete failure, the concrete failure precipitated the "premature" FRP rupture. Rotating the square inner steel tube reduced the vulnerability of the sandwiched concrete in the non-uniformly confined and compressed corner regions, leading to higher resistance and/or greater ductility of the FCSC column. The beneficial effects diminished with increasing eccentricity, partly due to yielding of the rotated inner steel tube on the tensile side as the material was further from the neutral axis of bending.

1. Introduction

Fiber-reinforced polymer (FRP) jackets are used to increase the strength and ductility of concrete columns by providing "passive confinement" to the concrete core under compression [1]. Lam and Teng [2] were among the first to propose a design procedure for circular FRP-confined concrete columns, and the majority of published studies have investigated the performance of such circular columns. Studies on square FRP-confined concrete columns [3–12] are not so extensive, especially those with inner steel tubes. Researchers [14–17] have also conducted experimental tests to investigate the behaviour of circular FRP-concrete-steel composite (FCSC) columns under combined bending and compression, or under eccentric compression, with very few studies [18] done on square FCSC columns under eccentric compression.

Finite element (FE) analyses are instrumental in overcoming the difficulties and limitations associated with laboratory studies, including clarifying the interaction mechanism between FRP, concrete, and steel members, distribution of axial stresses, and confining pressures over the section [13,19–25]. Izadi et al. [26] recently developed a refined concrete damage plasticity model (CDPM), which is capable of closely predicting the entire stress–strain path of the confined concrete column, whether the post-transition response is ascending or descending. The proposed model was implemented in ABAQUS [27] for the CDPM to analyze the circular and square FRP-confined concrete columns and square hybrid FCSC columns under concentric compression. The FE methodology includes a confinement dependent hardening/softening rule based on Yu et al.'s recommendation [20], a modified flow rule in which the dilation angle is defined as a function of the ratio of the confining pressure to the lateral strain [22], and a newly proposed confinement dependent damage parameter.

A number of researchers [28–29] have proposed three-dimensional (3D) FE methodologies for square or rectangular FRP-confined concrete columns under eccentric loading. However, these early methodologies do not incorporate an accurate constitutive model for concrete

---

* Corresponding author.
E-mail addresses: ai754@uowmail.edu.au (A. Izadi), lteh@uow.edu.au (L.H. Teh), aziza@uow.edu.au (A. Ahmed), polak@uwaterloo.ca (M.A. Polak).

under triaxial compression, which is essential for concrete under non-uniform confinement [19–25].

This paper presents the development of a FE methodology for analyzing square FCSC columns under concentric, mono-eccentric, or biaxial loading. The FE models are developed in ABAQUS [27] by using the authors' refined CDPM [26] and the FRP damage criteria available in the literature. The developed FE models are verified against the experimental results obtained by Izadi and Teh [30], involving four square FCSC columns loaded under concentric compression, twelve under mono-eccentric compression, and four under biaxial compression. This paper analyses the behaviour and strength of eccentrically loaded square FCSC columns having either typical or rotated inner steel tube configuration [26], and is not a parametric study.

2. Constitutive models

2.1. Constitutive model of FRP

Glass Fibre-Reinforced Polymer (GFRP) has high stiffness along the length of the fibers and low stiffness in the transverse direction. In the current study, the fibers of the GFRP tubes were along the hoop direction of the column. The hoop tensile stiffness of the GFRP tubes was therefore higher than its axial compressive stiffness. The elasticity model in ABAQUS was adopted for the GFRP tubes, which exhibit linearly elastic stress–strain behaviour.

Averaging from four flat coupon tests [30], the elastic modulus and rupture strain of the GFRP were found to be 30.5 GPa and 0.0218, respectively. Based on the manufacturer's data, the elastic modulus and the rupture strain of the GFRP are 27.6 GPa and 0.023, with a nominal layer thickness of 0.294 mm. Unless stated otherwise, the manufacturer's values were used in the FE modelling. In the transverse direction to the fibre (or the matrix direction), the elastic modulus is assumed to be 10 MPa so its contribution to the axial resistance is negligible.

2.1.1. Damage initiation of FRP

The inbuilt Hashin's damage criteria [31] in ABAQUS is used for modelling the FRP jacket. The initiation of FRP damage refers to the beginning of material degradation. Hashin's damage criteria include four different damage initiation mechanisms as follows:

Fiber tension ($\sigma_{11} \geqslant 0$)

$$F_f^t = \left(\frac{\sigma_{11}}{F_{1t}}\right)^2 + \alpha\left(\frac{\sigma_{12}}{F_6}\right)^2 \tag{1}$$

Fiber compression ($\sigma_{11} < 0$)

$$F_f^c = \left(\frac{\sigma_{11}}{F_{1c}}\right)^2 \tag{2}$$

Matrix tension and/or shear ($\sigma_{22} \geqslant 0$)

$$F_m^t = \left(\frac{\sigma_{22}}{F_{2t}}\right)^2 + \left(\frac{\sigma_{12}}{F_6}\right)^2 \tag{3}$$

Matrix compression ($\sigma_{22} < 0$)

$$F_m^c = \left(\frac{\sigma_{22}}{2F_4}\right)^2 + \left[\left(\frac{F_{2c}}{2F_4}\right)^2 - 1\right]\frac{\sigma_{22}}{F_{2c}} + \left(\frac{\sigma_{12}}{F_6}\right)^2 \tag{4}$$

where F_f^t, F_f^c, F_m^t and F_m^c are indexes showing the satisfaction of a damage initiation criterion when they exceed 1.0; σ_{ij} are the components of the stress tensor; F_{1t}, F_{1c}, are the tensile and compressive strengths in the fiber direction; F_{2t}, F_{2c}, are the tensile and compressive strengths in the matrix direction; F_4, F_6, are the transverse and longitudinal shear strengths; and α indicates the contribution of the shear stress to the fiber tensile criterion.

Barbero et al. [32] proposed $\alpha = 0$, used in the current study to ignore the shear stress effects on the fiber tensile criterion. Barbero et al. [32] used $F_4 = 0.5F_{2c}$ in their study. However, due to the negligible transverse shear strength and compressive strength in the matrix

Table 1
Manufacturer's data used for modelling the GFRP tube.

F_{1t}(MPa)	F_{1c}(MPa)	F_{2t}(MPa)	F_{2c}(MPa)	F_6(MPa)	F_4(MPa)
540	432	10	10	42	10

direction, these values are set equal to each other (i.e., $F_4 = F_{2c}$) in the current study. Details are provided in Table 1.

The damaged stiffness matrix c used to calculate $\sigma = C : \varepsilon$ is given by:

$$C = \begin{bmatrix} (1-d_f)E_1/\Delta & (1-d_f)(1-d_m)\nu_{21}E_1/\Delta & 0 \\ (1-d_f)(1-d_m)\nu_{12}E_2/\Delta & (1-d_m)E_2/\Delta & 0 \\ 0 & 0 & (1-d_s)G_{12} \end{bmatrix} \tag{5a}$$

$$\Delta = 1 - (1-d_f)(1-d_m)\nu_{12}\nu_{21} \tag{5b}$$

$$d_s = 1 - (1-d_f^t)(1-d_f^c)(1-d_m^t)(1-d_m^c) \tag{5c}$$

where σ is the apparent stress, ε is the strain; E_1 and E_2 are the moduli in the fiber direction and perpendicular to the fibers, respectively; G_{12} is the in-plane shear modulus; ν_{12} and ν_{21} are the in-plane Poisson's ratios; d_f^t, d_f^c, d_m^t, d_m^c and d_s are the damage variables for fiber in tension, fiber in compression, matrix in tension, matrix in compression, and shear damage mode, respectively. The damage variables d_f^t, d_f^c, d_m^t and d_m^c correspond to the four damage initiation modes in Equations (1)-(4). They can be reduced to two variables since material points are either in tension or compression at any time:

$$d_f = \begin{cases} d_f^t & \text{if } \sigma_{11} \geqslant 0 \\ d_f^c & \text{if } \sigma_{11} < 0 \end{cases} \tag{6}$$

and

$$d_m = \begin{cases} d_m^t & \text{if } \sigma_{22} \geqslant 0 \\ d_m^c & f \ \sigma_{22} < 0 \end{cases} \tag{7}$$

2.1.2. Damage evolution of FRP

The damage evolution criterion uses the effective stress $\widetilde{\sigma}$ instead of the apparent stress σ [33]:

$$\widetilde{\sigma} = M^{-1} : \sigma \tag{8a}$$

$$M^{-1} = \begin{bmatrix} (1-d_f)^{-1} & 0 & 0 \\ 0 & (1-d_m)^{-1} & 0 \\ 0 & 0 & (1-d_s)^{-1} \end{bmatrix} \tag{8b}$$

where M^{-1} is the damage effect tensor.

Before damage is initiated, the damage effect tensor is equal to the identity tensor. When any of the damage initiation criteria, i.e. Equations (1)-(4), is satisfied, the material stiffness degradation is triggered. The evolution of each damage variable is governed by an equivalent displacement δ_{eq}^I ($I = ft, fc, mt, mc$) [32]:

Fiber tension ($\sigma_{11} \geqslant 0$)

$$\delta_{eq}^{ft} = L^C \sqrt{\langle \varepsilon_{11} \rangle^2 + \alpha \varepsilon_{12}^2} \tag{9a}$$

$$\sigma_{eq}^{ft} = \frac{\langle \sigma_{11} \rangle \langle \varepsilon_{11} \rangle + \alpha \sigma_{12} \varepsilon_{12}}{\delta_{eq}^{ft}/L^C} \tag{9b}$$

Fiber compression ($\sigma_{11} < 0$)

$$\delta_{eq}^{fc} = L^C \langle -\varepsilon_{11} \rangle \tag{10a}$$

$$\sigma_{eq}^{fc} = \frac{\langle -\sigma_{11} \rangle \langle -\varepsilon_{11} \rangle}{\delta_{eq}^{fc}/L^C} \tag{10b}$$

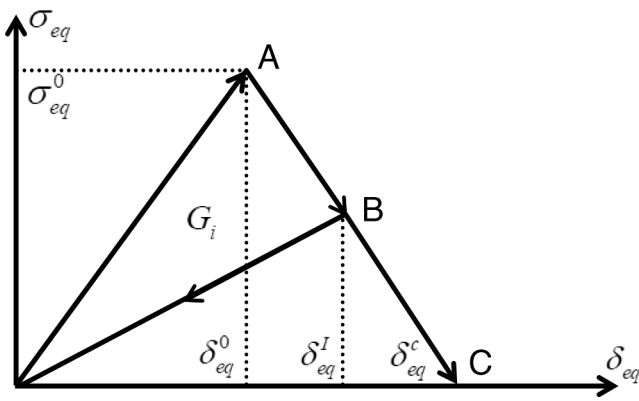Matrix tension and/or shear ($\sigma_{22} \geqslant 0$)

Fig. 1. Damage evolution behaviour of a linearly softening material.

$$\delta_{eq}^{mt} = L^C \sqrt{\langle \varepsilon_{11} \rangle^2 + \varepsilon_{12}^2} \tag{11a}$$

$$\sigma_{eq}^{mt} = \frac{\langle \sigma_{22} \rangle \langle \varepsilon_{22} \rangle + \sigma_{12} \varepsilon_{12}}{\delta_{eq}^{mt}/L^C} \tag{11b}$$

Matrix compression ($\sigma_{22} < 0$)

$$\delta_{eq}^{mc} = L^C \sqrt{\langle -\varepsilon_{22} \rangle^2 + \varepsilon_{12}^2} \tag{12a}$$

$$\sigma_{eq}^{mc} = \frac{\langle -\sigma_{22} \rangle \langle -\varepsilon_{22} \rangle + \sigma_{12} \varepsilon_{12}}{\delta_{eq}^{mc}/L^C} \tag{12b}$$

where $\langle \square \rangle$ represents the Macaulay operator that is defined as $\langle x \rangle = \frac{1}{2}(x + |x|)$ for every $x \in \Re$. The superscripts *ft*, *fc*, *mt* and *mc* denote the four damage modes: fiber tension, fiber compression, matrix tension, and matrix compression, respectively; σ_{eq} is the equivalent stress value corresponding to the equivalent displacement for a linearly softening material; and L^C is the characteristic length of the membrane and shell elements, which is the square root of the area of the reference surface of the element.

The damage variable d_I ($I = ft, fc, mt, mc$) for each failure mode is:

$$d_I = \frac{\delta_{eq}^c (\delta_{eq}^I - \delta_{eq}^0)}{\delta_{eq}^I (\delta_{eq}^c - \delta_{eq}^0)} \tag{13}$$

where δ_{eq}^I is the equivalent displacement based on a particular failure mode (i.e. Equations (9)-(12)), δ_{eq}^c is the equivalent displacement at the complete damage state of the FRP, and δ_{eq}^0 is the initial equivalent displacement at which the damage initiation criterion is satisfied. Fig. 1 shows the bilinear damage evolution model used for the materials having a linear softening behaviour. The parameter δ_{eq}^0 depends on the elastic stiffness and strength, and the parameter δ_{eq}^c depends on the fracture toughness.

The fracture energy parameters govern the post failure slope of the unloading process. Due to the absence of experimental data, the fracture energy values in Table 2 were obtained from the literature [34–37] for the same material and were applied in the current FE analyses. In Table 2, the fracture energy parameters G_{Lt}, G_{Lc}, G_{Tt}, and G_{Tc} are the longitudinal tensile, longitudinal compressive, transverse tensile, and transverse compressive fracture energies. The dissipated fracture energies specify the yielding after the damage initiation.

In Table 2, η_{Lt}, η_{Lc}, η_{Tt} and η_{Tc} are the input parameters for the viscosity coefficients in the longitudinal tensile, longitudinal compressive, transverse tensile, and transverse compressive directions. Small values of viscosity coefficients are recommended in order to reduce the convergence difficulties caused by the stiffness degradation of an element and the softening behaviour [35,38]. Different values of viscosity coefficients have been trialed in the analyses and a value of 0.0004 is adopted for the fiber and the matrix viscosity coefficients.

The FRP damage initiation and evolution criteria employed in the present work are evaluated in Section 3.3.

2.2. Constitutive models of steel and concrete

The classical plasticity model based on the J_2 flow theory is used for the steel tubes with isotropic hardening. The experimental tensile stress–strain results were extracted from the steel coupon tests to define the true stress–strain curve using the Ramberg-Osgood parameters [39]. Four flat coupons were cut from different sides of the steel tube and used in the standard tensile tests [40]. The average elastic modulus, yield stress and ultimate tensile strength are 202 GPa, 425 MPa and 460 MPa, respectively. The Poisson's ratio is assumed to be 0.3.

In this study, the refined Concrete Damaged Plasticity (CDPM) model [26] is applied to analyze the concrete behaviour under eccentric compression. The compression hardening/softening rule is a function of the confining pressure based on Yu et al.'s recommendation [20]. The dilation angle is defined as a function of the ratio of the confining pressure to the lateral strain [22]. The confinement dependent concrete damage parameter d proposed by Izadi et al. [26] is:

$$d = \phi \begin{cases} 1 - \dfrac{f_{cc}' * n}{E_c \varepsilon_{cc}^* \left[n - 1 + \left(\dfrac{\varepsilon_c}{\varepsilon_{cc}^*} \right)^{1.095n} \right]}, & \dfrac{\varepsilon_c}{\varepsilon_{cc}^*} \leqslant 1 \\[4mm] 1 - \dfrac{f_{cc}' *}{E_c \varepsilon_{cc}^* \left[\alpha_c \left(\dfrac{\varepsilon_c}{\varepsilon_{cc}^*} - 1 \right)^2 + \dfrac{\varepsilon_c}{\varepsilon_{cc}^*} \right]}, & \dfrac{\varepsilon_c}{\varepsilon_{cc}^*} > 1 \end{cases} \tag{14a}$$

$$\alpha_c = 27/f_{cc}' *; n = \frac{E_c \varepsilon_{cc}^*}{E_c \varepsilon_{cc}^* - f_{cc}' *} \tag{14b}$$

$$\frac{f_{cc}' *}{f_{co}'} = 1 + 3.5 \frac{\sigma_{l,eff}}{f_{co}'} \tag{14c}$$

$$\frac{\varepsilon_{cc}^*}{\varepsilon_{co}} = 1 + 17.5 \frac{\sigma_{l,eff}}{f_{co}'} \tag{14d}$$

$$\sigma_{l,eff} = \frac{2(\sigma_2 + 0.039 f_{co}')(\sigma_3 + 0.039 f_{co}')}{(\sigma_2 + \sigma_3 + 0.078 f_{co}')} - 0.039 f_{co}' \tag{14e}$$

where ϕ is a reduction factor equal to 0.6, $f_{cc}' *$ and ε_{cc}^* are the peak compressive stress and the corresponding strain under the effective confining pressure $\sigma_{l,eff}$. The variables σ_2 and σ_3 are the orthogonal principal lateral stresses of the concrete. Based on Yu et al.'s recommendation [20], the value of $A = 0.12$ is adopted in this study. The value of $C = 1.83$ is used based on the experimental shear strength ratio of concrete between biaxial compression and triaxial compression [20]. f_{co}' is the unconfined concrete strength, ε_{co} is the axial strain at the peak axial stress of the unconfined concrete set to $\varepsilon_{co} = 0.000937 \sqrt[4]{f_{co}'}$ [41], ε_c

Table 2
Damage evolution (fracture energies) and stabilization parameters of the FRP.

Damage evolution				Damage stabilization			
G_{Lt}(N/mm)	G_{Lc}(N/mm)	G_{Tt}(N/mm)	G_{Tc}(N/mm)	η_{Lt}	η_{Lc}	η_{Tt}	η_{Tc}
12.5	12.5	1	1	0.0004	0.0004	0.0004	0.0004

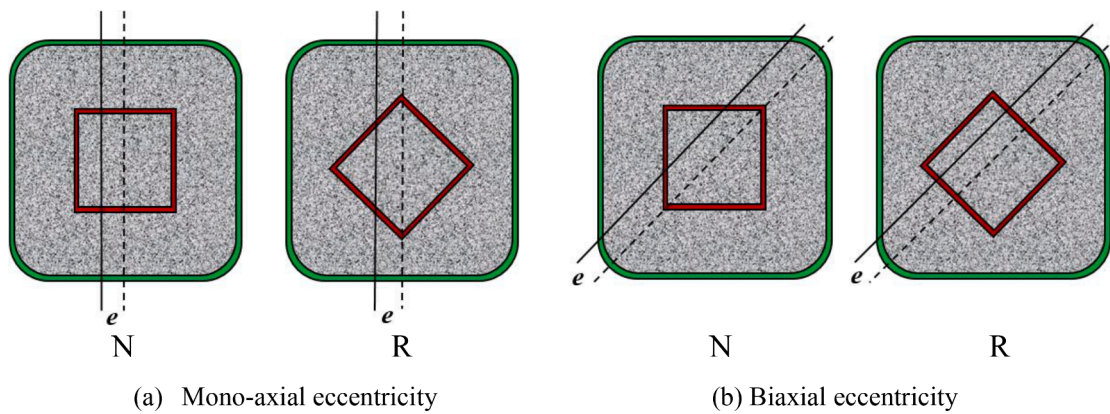(a) Mono-axial eccentricity   (b) Biaxial eccentricity

Fig. 2. Tested and analysed configurations.

Table 3
Test specimens [30] analysed in this paper.

Configuration	Steel tube (mm)	e (mm)
N-125	125 × 125 × 4	0
R-125	125 × 125 × 4	0
N-150	150 × 150 × 5	0
R-150	150 × 150 × 5	0
NE-125-20	125 × 125 × 4	20
RE-125-20	125 × 125 × 4	20
NE-125-35	125 × 125 × 4	35
RE-125-35	125 × 125 × 4	35
NE-150-35	150 × 150 × 5	35
RE-150-35	150 × 150 × 5	35
NB-150-35	150 × 150 × 5	35
RB-150-35	150 × 150 × 5	35

is the axial strain of concrete, and E_c is the elastic modulus of the unconfined concrete set to $E_c = 4730\sqrt{f'_{co}}$ (f'_{co} in MPa) [42]. More details of refinements applied to the CDPM model are provided in Izadi et al. [26].

To apply the refinements in ABAQUS [27], the in-built field variables

f_1 and f_2 are specified by providing a link between the FE software and a FORTRAN subroutine. The field variable f_1 includes the ratio of the confining pressure to the lateral strain values, and f_2 contains the confining pressure values. The relationship between the field variables is defined in the user subroutine USDFLD coded in FORTRAN.

The concrete material of the specimens analysed in this paper had an average unconfined strength f'_{co} of 56.7 MPa as obtained from the standard cylinder tests [43]. The Poisson's ratio is assumed to be 0.15.

3. FE modelling and analysis of square FCSC beam-columns

3.1. Test specimens [30] analysed in this paper

Fig. 2 shows the cross-section configurations of the 850 mm long, 225 mm wide square concrete columns tested by Izadi and Teh [30] under combined bending and compression. The eccentric e and other variables of the twenty FCSC specimens analyzed in this paper are given in Table 3. The designations N and R in the specimen labels denote the "normal" and the "rotated" inner steel tube configurations shown in Fig. 2, respectively, while E and B denote the mono-axial and the biaxial
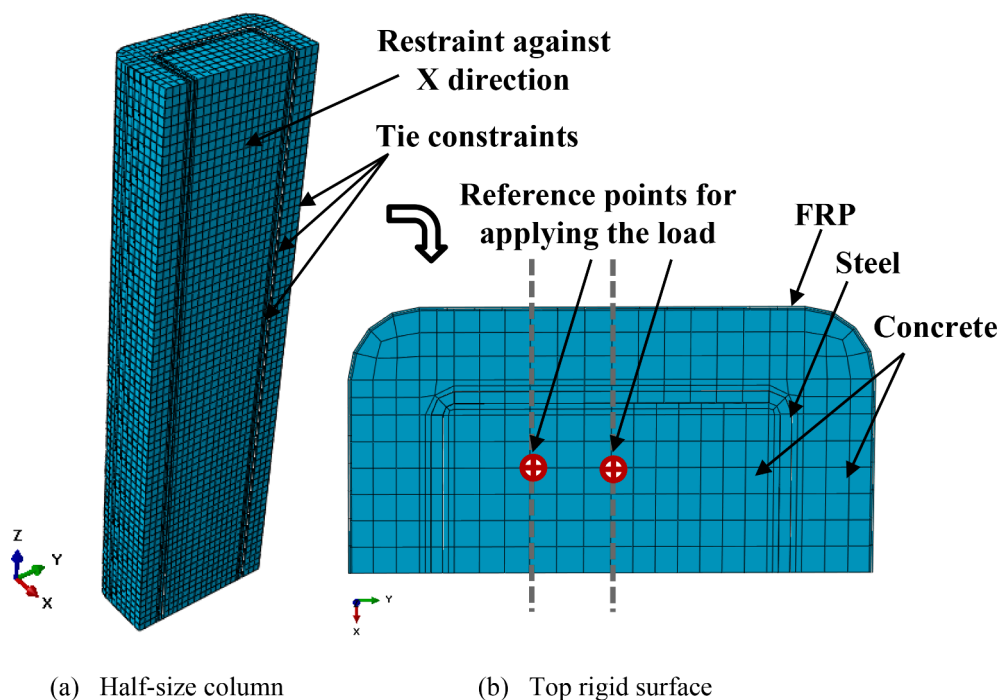

(a) Half-size column   (b) Top rigid surface

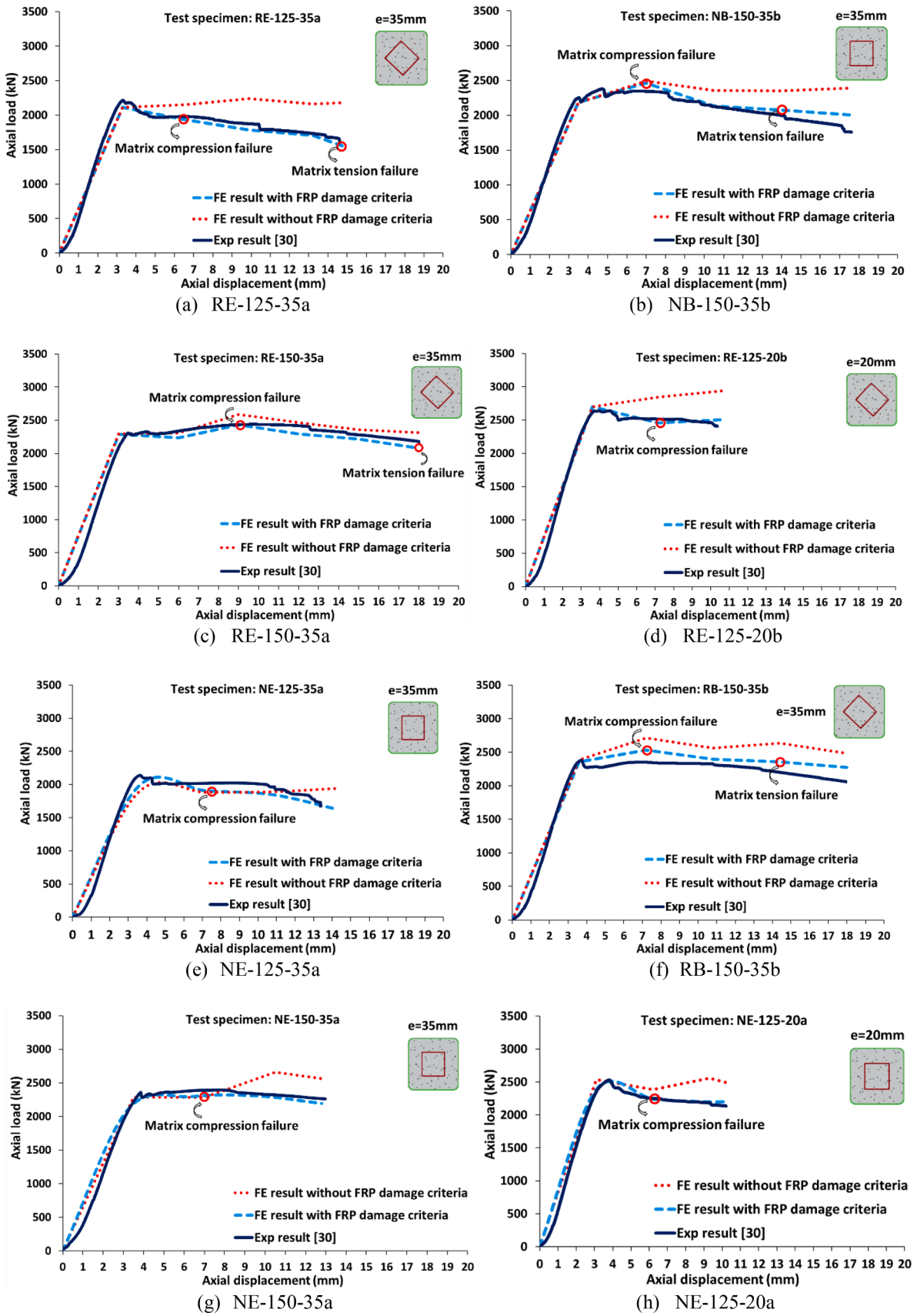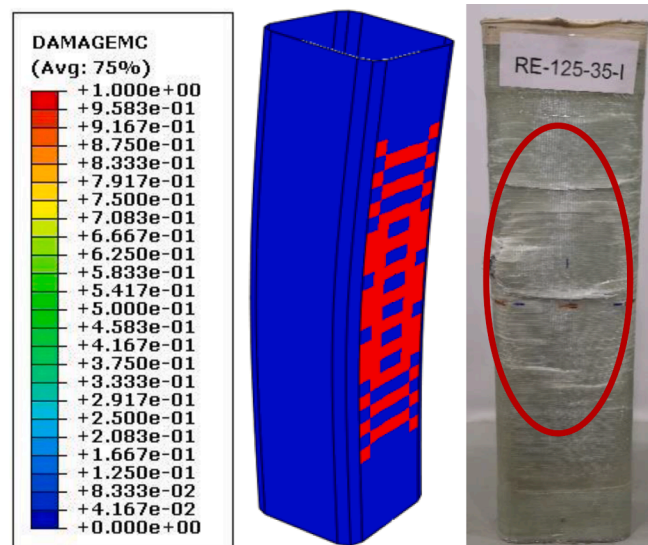**Fig. 3.** Square FCSC under eccentric compression.

Fig. 4. Effects of FRP damage criteria on FE analysis results.

(a) GFRP matrix failure on the compressive side

(b) GFRP matrix failure on the tensile side

Fig. 5. Specimen RE-125-35a at the test termination point.

loading conditions, respectively. All specimens had a corner radius of 30 mm, and were confined with five layers of GRFP.

3.2. The basic FE model

Fig. 3 shows the FE model for a square FCSC under mono-axial eccentric compression, which takes advantage of symmetry [44–45]. The tie constraints option in ABAQUS [27] was used to simulate the interaction between the steel tube's outer side and the concrete cover (sandwiched concrete) and the steel tube's inner side and the concrete core. The tie constraint is also adopted to simulate the interaction between the concrete and the FRP tube. A compressive load is applied to the top nodes by prescribing axial displacements there while the bottom surface is restrained against axial displacement. The concrete circumference is taken as the master of the inner surface of FRP in the Tie option, which is assumed to provide perfect bonding between the FRP and the concrete for a "no-slip" simulation [46]. There are five integration points along the thickness of the FRP jacket.

The eight-node reduced-integration brick element (C3D8R) [27] was used to model the concrete core, the sandwiched concrete and the steel tube. The concrete's mesh size was set to 12 mm following a mesh convergence study using 20, 16, 14, 12, and 10 mm meshes. Ignoring the flexural stiffness of the surrounding FRP sheets in the longitudinal direction of the columns, the four-node quadrilateral membrane element (M3D4R) [27] is used for modelling the FRP tube. This measure reduces the possibility of convergence difficulties usually caused by shell elements while avoiding the use of brick elements.

In the post-processing phase, the symmetric model can be mirrored to produce a whole model in order to facilitate visualization of the FE analysis outputs.

### 3.3. FRP damage simulation results

Fig. 4 demonstrates both the necessity and the accuracy of the FRP damage initiation and evolution criteria described in Section 2.1. It can be seen that the FE model employing the FRP damage criteria resulted in
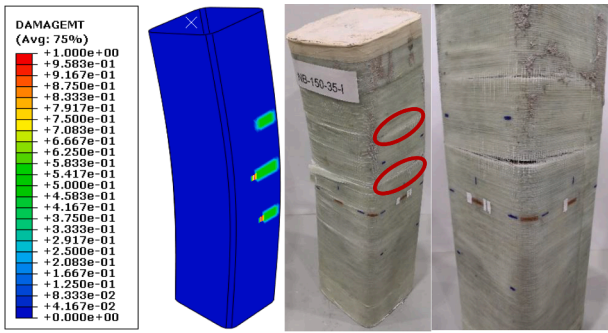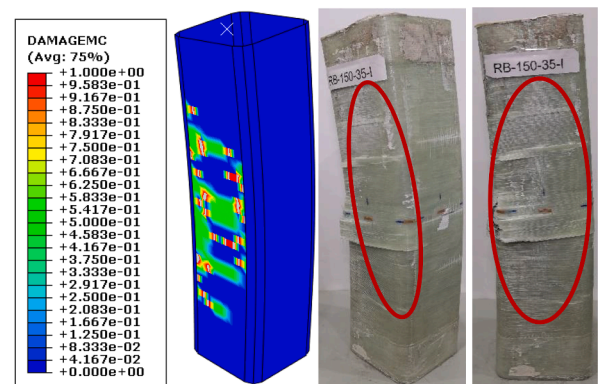
(a) GFRP matrix failure on the tensile side of Specimen NB-150-35a
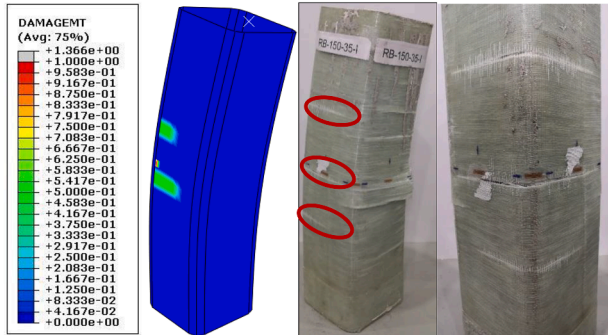
(b) GFRP matrix failure on the tensile side of Specimen RB-150-35a
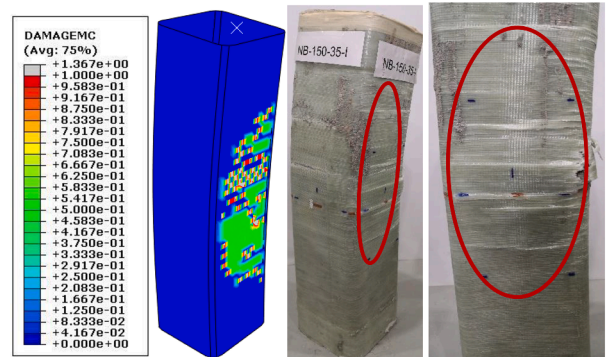
(c) GFRP matrix failure on the compressive side of Specimen NB-150-35a

(d) GFRP matrix failure on the compressive side of Specimen RB-150-35a

Fig. 6. Biaxially tested specimens at the test termination point.

Table 4

Apparent FRP hoop strains (at critical corners) at the test termination point.

Specimen	$\varepsilon_{term,test}$	$\varepsilon_{term,FEA}$
N-125a	0.0064	0.0058
R-125b	0.0052	0.0057
N-150a	0.0030	0.0032
R-150a	0.0064	0.0061
NE-125-20a	0.0080	0.0076
RE-125-20b	0.0065	0.0067
NE-125-35a	0.0055	0.0050
RE-125-35a	0.0057	0.0056
NE-150-35a	0.0035	0.0041
RE-150-35a	0.0069	0.0076
NB-150-35b	0.0047	0.0049
RB-150-35b	0.0060	0.0055

much closer agreements with the test results [30] than the model without the damage criteria. The first detections of complete damage (failure) of the GFRP matrix are indicated in the figures.

It can be seen that GFRP matrix failure occurred on the compressive side of all the eccentrically loaded columns, and preceded the failure on the tensile side if the latter took place at all. It is also evident that while the column's resistance invariably declined following a GFRP matrix compression failure, such a failure did not immediately lead to the sudden loss of the column's load-carrying capacity. On the other hand, the sudden loss of a column's capacity was not always preceded by a GFRP matrix tension failure, especially for the specimens with mono-axial eccentricity.

Fig. 5 shows the FE simulation results for Specimen RE-125-35a at the test termination point, which are consistent with the experimental observations. The results shown in the figure are also consistent with the indications of Fig. 4(a), which show that the first matrix compression failure occurred early while the matrix tension failure only took place at the termination point. It can be seen from Fig. 5(a) that the FE simulation predicts multiple matrix compression failures, as did occur in the experimental test. On the other hand, Fig. 5(b) shows that the FE simulation predicts only one matrix tension failure, also consistent with the test result.

However, Fig. 4(b) and 4(f) indicate that the first GFRP matrix tension failures occurred well before the respective termination points of the two biaxial specimens NB-150-35b and RB-150-35b, suggesting the likelihood of multiple matrix tension failures. In fact, Fig. 6(a) and 6(b) show the occurrence of multiple matrix tension failures in the two specimens, both in the FE simulations and in the experimental tests.

It should be noted that the violent FRP rupture at the termination point typically occurred at a corner on the compressive side. The matrix compression failures of the two specimens are shown in Fig. 6(c) and 6(d). However, the FE analyses indicated that the columns had not experienced GFRP rupture (fiber in tension) at the test termination point according to the criteria described in Section 2.1. The FE results are in fact consistent with the experimental FRP hoop strains at the termination point obtained from the strain gauges at the ruptured corners, as shown in Table 4. The experimental and FE hoop strains at the test termination point are typically less than one third of the manufacturer's value of 0.023 for the GFRP's rupture strain, or, for that matter, the value of 0.0218 obtained by the authors through flat coupon tests [30]. It is also noteworthy that the hoop strain at the termination point of Specimen R-150 was about double that of Specimen N-150, as was the case with Specimens RE-150-35 and NE-150-35.

3.4. Concrete behavior and the hoop strain

The hoop strain-axial strain curves obtained by the present FE analyses are compared with the experimental results of the FCSC columns [30] in Fig. 7. The experimental corner hoop strain values are the average taken from the four horizontal strain gauges (with a gauge length of 20 mm) on the rounded corners in the mid-height region of the

(a) Specimen N-125a

(b) Specimen R-125b

(c) Specimen N-150a

(d) Specimen R-150b

(e) Specimen NE-125-20a

(f) Specimen NE-125-35a

(g) Specimen RE-125-20b

(h) Specimen RE-125-35a

(i) Specimen NB-150-35b

(j) Specimen RB-150-35b
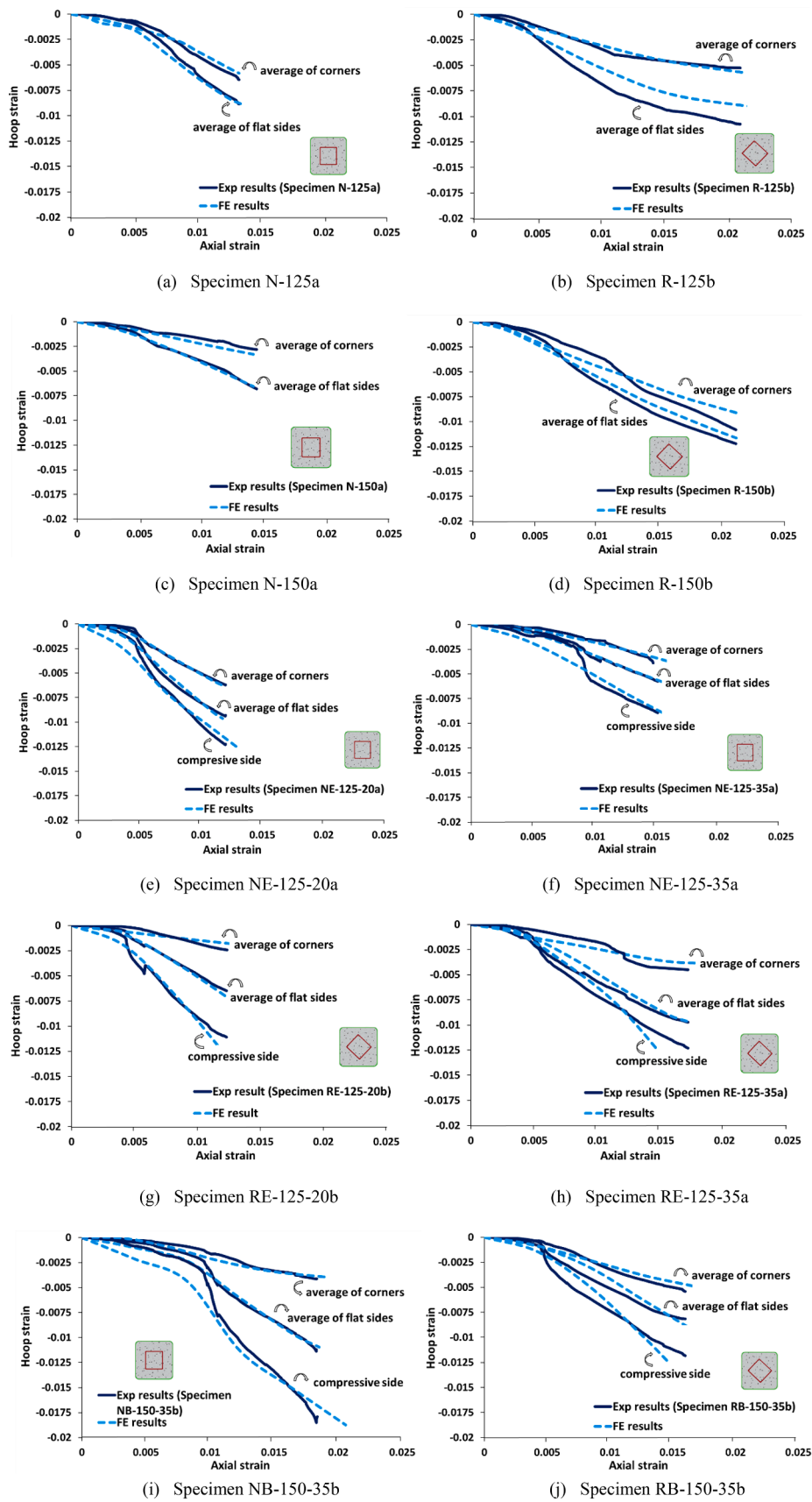
Fig. 7. Hoop strain-axial strain verification results.

(a) Specimens RE-125-20b and NE-125-20a (mono-axial eccentricity)

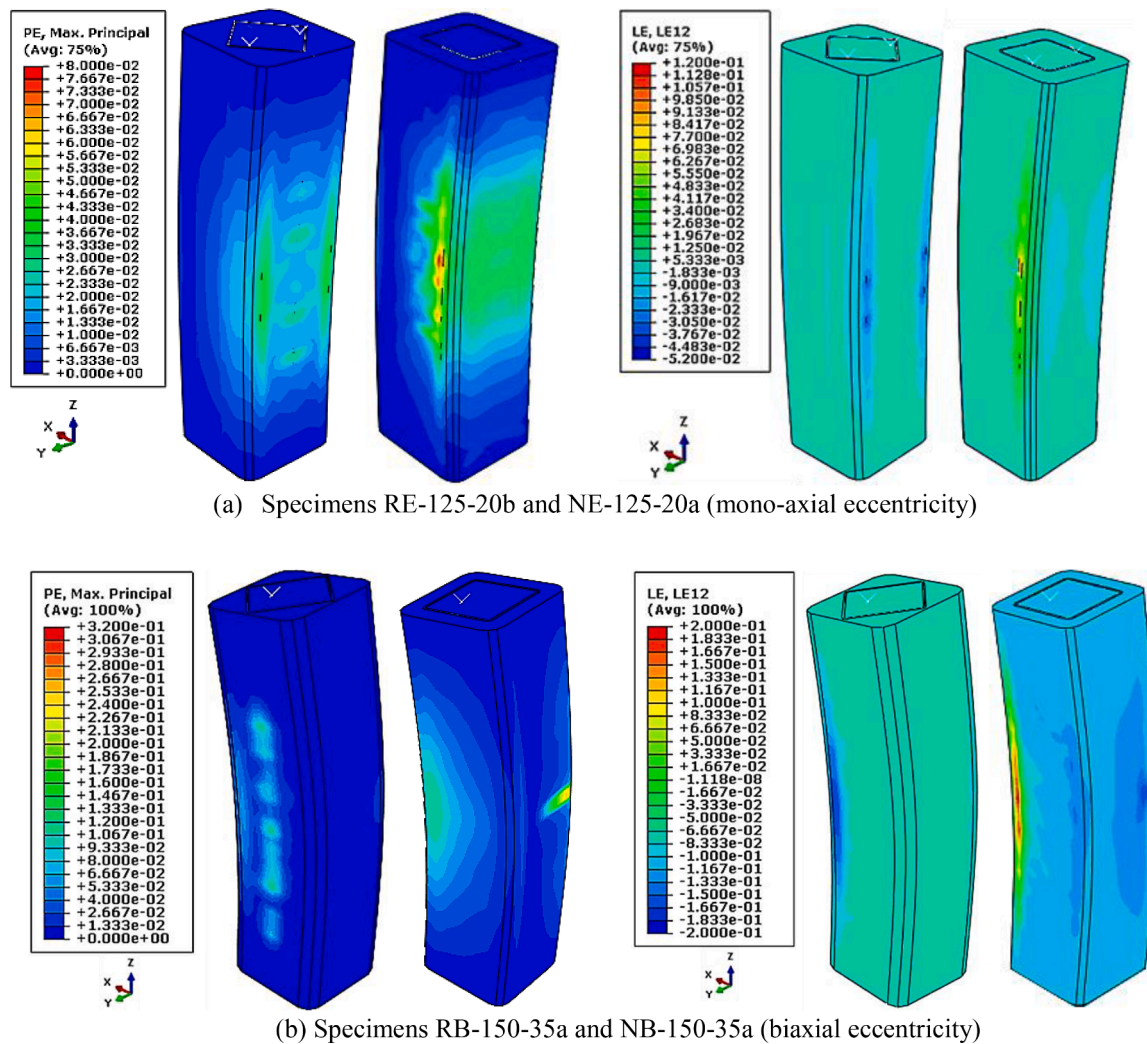(b) Specimens RB-150-35a and NB-150-35a (biaxial eccentricity)

Fig. 8. Maximum principal strains and shear strains at the same axial displacements.

column. Similarly, the experimental flat side hoop strain values are the average of the four horizontal strain gauges on the flat sides in the mid-height region. The axial strain values are the average from two full-length LVDTs.

Fig. 7 shows that the FE hoop strain-axial strain curves are consistent with those observed in the tests, although there were a few instances where the experimental curve did not follow the expected trend. Since the FRP hoop strain is related to the concrete expansion under axial compression, the comparison results should provide confidence that the constitutive model described in Section 2.2 is reasonably accurate, consistent with the earlier finding [26] and supported by the FRP simulation results discussed in the preceding subsection.

Comparisons of the maximum principal plastic strains and the shear strains of the concrete columns are presented in Fig. 8 for the normal and the rotated steel tube configurations. Each comparison is made at the same axial displacements corresponding to the termination point of the normal specimen. It can be seen that, for both the mono-axial and the bi-axial eccentric loading cases of the respective 125-mm and 150-mm columns, the concrete columns with the normally orientated steel tube are more vulnerable to failure than their rotated counterparts.

As shown in Fig. 8, the most vulnerable region of each column is the corner, where the sandwiched concrete is the most confined in the di-agonal direction of the cross-section. In fact, FRP ruptures in square columns have been observed to take place at the corners [6–8,30,47] rather than the more strained flat sides. This finding coupled with the

previous discussions on the results of Table 4 suggests the possibility that, rather than the FRP rupture leading to concrete failure in an FRP confined concrete column, the concrete failure precipitates the FRP rupture. Since the concrete failure is violent, the strain gauges cannot capture the actual rupture strain of the FRP, which could explain why the rupture strain values obtained from column tests are typically much lower than those from standard coupon tests [2,48].

3.5. Effects of inner steel tube's orientation and size

Fig. 9 shows the axial load–displacement curves obtained in the present FE analyses are reasonably close to the laboratory test results [30]. Coupled with the verification results discussed in the preceding subsections, the present FE methodology is considered validated, and the results can be reliably used to interpret the column behaviour.

It can be seen from Fig. 9 that the rotated steel configuration is generally superior to the normal alternative, leading to higher resistance and/or greater ductility of the hybrid column. In fact, Fig. 9(a) shows that rotating the 125-mm inner steel tube led to a greater ductility than using the 150-mm steel tube, although the larger steel tube afforded a slightly higher resistance at the transition point (not at column failure).

The beneficial effects of the rotated inner steel tube diminished with increased load eccentricity, as evident from Fig. 9(b) through (d). Nevertheless, Fig. 9(b) shows that the rotated configuration still led to greater ductility for the load eccentricity of 35 mm, to the same extent as
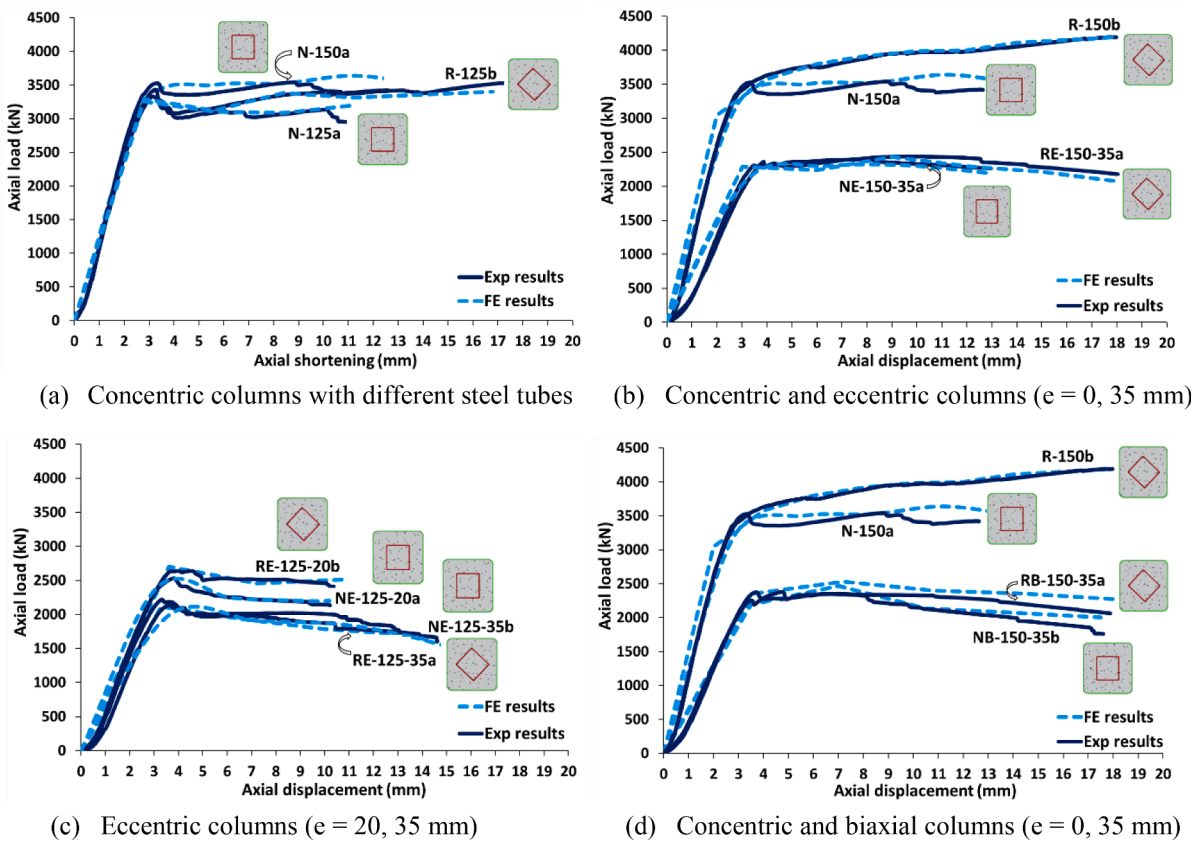
(a) Concentric columns with different steel tubes

(b) Concentric and eccentric columns (e = 0, 35 mm)

(c) Eccentric columns (e = 20, 35 mm)

(d) Concentric and biaxial columns (e = 0, 35 mm)

Fig. 9. Effects of steel tube's orientation and size.

(a) Specimens NE-125-20a and RE-125-20b
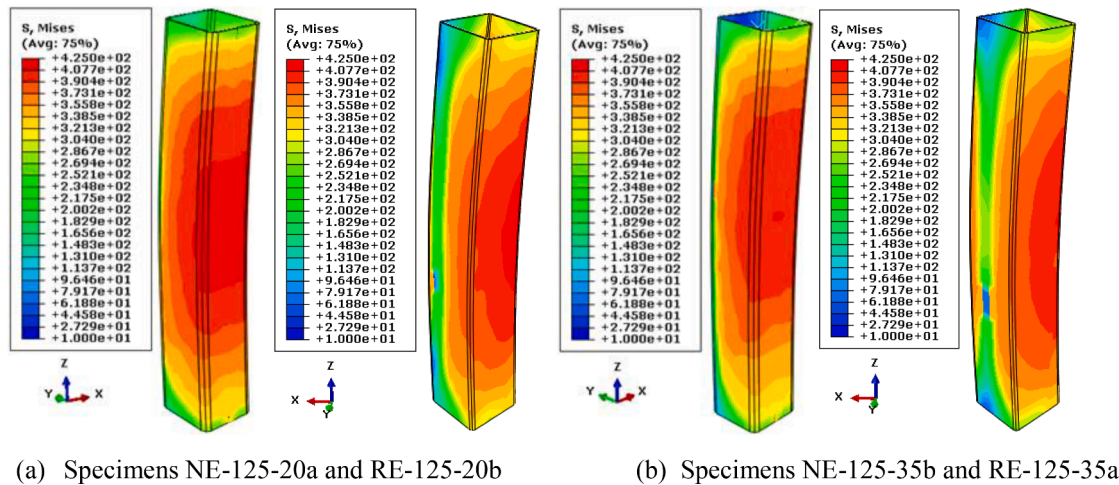
(b) Specimens NE-125-35b and RE-125-35a

Fig. 10. The von Mises stresses of the inner steel tubes.

for the concentric loading case. On the other hand, Fig. 9(d) shows the higher resistance of the rotated configuration under biaxial loading. The rotated configuration also led to higher resistance for the columns under the load eccentricity of 20 mm, as shown in Fig. 9(c).

The von Mises stress contours on the compressive side of the steel tubes corresponding to the axial displacement at the termination point of the respective normal configuration specimens are presented in Fig. 10. It can be seen from Fig. 10(a) that the rotated steel tube of Specimen RE-125-20b is subjected to significantly less yielding than its normal counterpart, which is consistent with the results in Fig. 9(c) showing the higher resistance of the rotated specimen.

On the other hand, Fig. 10(b) shows that the tensile side of the

rotated steel tube in Specimen RE-125-35a is subjected to more yielding than its normal counterpart, which explains why the rotated steel tube did not lead to better performance. The reason for the more extensive yielding under the larger eccentricity is that the tensile corner of the rotated tube was farther from the neutral axis compared to the normally placed tube.

4. Conclusions

The paper has presented the FE analysis of square FRP-concrete-steel composite (FCSC) columns under concentric and eccentric loadings, and validated the developed FE methodology against experimental test

results. The FE model was able to replicate the GFRP matrix compression and tension failures in addition to accurately tracing the load–deflection path beyond the transition point. The FE analysis was used in this paper to investigate the strain patterns of the sandwiched concrete under different orientations of the inner steel tube.

The most vulnerable region of each column was shown to be the corner, where the sandwiched concrete was the most confined in the diagonal direction of the cross-section. Failures of the test columns in fact typically started at a corner even though the hoop strain there was significantly lower than at the flat sides of the square column. Rotating the inner steel tube reduces the vulnerability of the sandwiched concrete in the non-uniformly confined and compressed corner regions, leading to higher resistance and/or greater ductility of the FCSC column. The beneficial effects diminished with increasing eccentricity, partly due to yielding of the rotated inner steel tube on the tensile side as the material was further from the neutral axis of bending.

When a column suddenly failed, the GFRP hoop strain at the failed corner was found through experimental measurement as well as FE analysis to be typically less than one third of the rupture strain obtained from flat coupon tests, and as low as 15%. Furthermore, among the tested columns, the hoop strains at column failure varied by up to 100% even though the same GFRP material was used. These observations, coupled with those described in the second paragraph of this section, suggest that it was the concrete failure that led to the FRP rupture rather than the other way round, as believed in the literature. Further research is required to confirm this indication.

Under combined bending and compression, GFRP matrix compression failure invariably occurred on the compressive side of the FCSC column, and preceded the matrix tension failure if the latter occurred at all. Neither matrix failure immediately led to a sudden loss of the test column's load-carrying capacity.

The developed FE methodology can be used for future parametric studies of square FRP-concrete-steel columns under concentric and eccentric loadings. Such studies are often required in order to derive strength equations for use in structural design. However, more verifications against experimental test results of square FCSC columns having very different configurations may be needed to identify potential limitations of the presented FE methodology.

Declaration of Competing Interest

The authors declare that they have no known competing financial interests or personal relationships that could have appeared to influence the work reported in this paper.

Acknowledgment

References

[1] ACI (American Concrete institute). Guide for the design and construction of externally bonded FRP systems for strengthening concrete structures ACI 440.2R-17 2017 Farmington Hills, MI.

[2] Lam L, Teng JG. Ultimate condition of fiber reinforced polymer-confined concrete. J Compos Constr 2004;8(6):539–48.

[3] Mirmiran A, Shahawy M, Samaan M, Echary HE, Mastrapa JC, Pico O. Effect of column parameters on FRP-confined concrete. J Compos Constr 1998;2(4):175–85.

[4] Rochette P, Labossiere P. Axial testing of rectangular column models confined with composites. J Compos Constr 2000;4(3):129–36.

[5] Wang YF, Wu HL. Experimental investigation on square high-strength concrete short columns confined with AFRP sheets. J Compos Constr 2010;14(3):346–51.

[6] Ozbakkaloglu T. Compressive behavior of concrete-filled FRP tube columns: Assessment of critical column parameters. Eng Struct 2013;51:188–99.

[7] Ozbakkaloglu T. Behavior of square and rectangular ultra high-strength concrete-filled FRP tubes under axial compression. Compos B Eng 2013;54:97–111.

[8] Fanggi BA, Ozbakkaloglu T. Square FRP–HSC–steel composite columns: Behavior under axial compression. Eng Struct 2015;92:156–71.

[9] Ozbakkaloglu T, Xie T. Geopolymer concrete-filled FRP tubes: Behavior of circular and square columns under axial compression. Compos B Eng 2016;96:215–30.

[10] Saleem S, Hussain Q, Pimanmas A. Compressive behavior of PET FRP–confined circular, square, and rectangular concrete columns. J Compos Constr 2017;21(3):04016097.

[11] de Diego A, Arteaga Á, Fernández J. Strengthening of square concrete columns with composite materials. Investigation on the FRP jacket ultimate strain. Compos B Eng 2019;162:454–60.

[12] Huang J, Li T, Zhu D, Gao P, Zhou A. Compressive behavior of circular and square concrete column externally confined by different types of basalt fiber–reinforced polymer. Adv Struct Eng 2020;23(8):1534–47.

[13] Lin G, Teng JG. Three-dimensional finite-element analysis of FRP-confined circular concrete columns under eccentric loading. J Compos Constr 2017;21(4):04017003.

[14] Yu T, Wong YL, Teng JG. Behavior of hybrid FRP-concrete-steel double-skin tubular columns subjected to eccentric compression. Adv Struct Eng 2010;13(5):961–74.

[15] Zakaib S, Fam A. Flexural performance and moment connection of concrete-filled GFRP tube–encased steel I-sections. J Compos Constr 2012;16(5):604–13.

[16] Yao J, Jiang T, Xu P, Lu ZG. Experimental investigation on large-scale slender FRP-concrete-steel double-skin tubular columns subjected to eccentric compression. Adv Struct Eng 2015;18(10):1737–46.

[17] Yu T, Lin G, Zhang SS. Compressive behavior of FRP-confined concrete-encased steel columns. Compos Struct 2016;154:493–506.

[18] Huang Le, Yu Tao, Wang Zhen-Yu, Zhang Shi-Shun. Compressive behaviour of slender FRP-confined concrete-encased cross-shaped steel columns. Constr Build Mater 2020;258:120356.

[19] Yu T, Teng JG, Wong YL, Dong SL. Finite element modeling of confined concrete-I: Drucker-Prager type plasticity model. Eng Struct 2010;32(3):665–79.

[20] Yu T, Teng JG, Wong YL, Dong SL. Finite element modeling of confined concrete-II: Plastic-damage model. Eng Struct 2010;32(3):680–91.

[21] Lo SH, Kwan AK, Ouyang Y, Ho JC. Finite element analysis of axially loaded FRP-confined rectangular concrete columns. Eng Struct 2015;100:253–63.

[22] Hany NF, Hantouche EG, Harajli MH. Finite element modeling of FRP-confined concrete using modified concrete damaged plasticity. Eng Struct 2016;125:1–14.

[23] Farahmandpour C, Dartois S, Quiertant M, Berthaud Y, Dumontet H. A concrete damage–plasticity model for FRP confined columns. Mater Struct 2017;50(2):1–7.

[24] Chellapandian M, Prakash SS, Rajagopal A. Analytical and finite element studies on hybrid FRP strengthened RC column elements under axial and eccentric compression. Compos Struct 2018;184:234–48.

[25] Rasouli M, Broujerdian V. 3D finite element modeling of FRP-confined rectangular short columns considering variation of Poisson's ratio. Iranian J Sci Technol, Trans Civil Eng 2020;44(2):449–61.

[26] Izadi A, Teh LH, Polak MA, Ahmed A. Finite element analysis of square FRP-concrete-steel columns under concentric compression. Structures 2022;44:1312–20.

[27] ABAQUS. v. 6.14-2 [Computer software]. Dassault Systèmes, Waltham, MA 2014.

[28] Parvin A, Wang W. Behavior of FRP jacketed concrete columns under eccentric loading. J Compos Constr 2001;5(3):146–52.

[29] Hu B, Wang JG, Li GQ. Numerical simulation and strength models of FRP-wrapped reinforced concrete columns under eccentric loading. Constr Build Mater 2011;25(5):2751–63.

[30] Izadi A, Teh LH, Ahmed A. Square FRP-concrete-steel composite columns under combined bending and compression. Manuscript in preparation, 2022.

[31] Hashin Z, Rotem A. A fatigue failure criterion for fiber reinforced materials. J Compos Mater 1973;7(4):448–64.

[32] Barbero EJ, Cosso FA, Roman R, Weadon TL. Determination of material parameters for Abaqus progressive damage analysis of E-glass epoxy laminates. Compos B Eng 2013;46:211–20.

[33] Barbero EJ. Finite element analysis of composite materials. CRC Press; 2007.

[34] Alfano G, Crisfield M. Finite element interface models for the delamination analysis of laminated composites: mechanical and computational issues. Int J Numer Meth Eng 2001;50(7):1701–36.

[35] Lapczyk I, Hurtado JA. Progressive damage modeling in fiber-reinforced materials. Compos A Appl Sci Manuf 2007;38(11):2333–41.

[36] Binienda WK, Li X. Mesomechanical model for numerical study of two-dimensional triaxially braided composite. J Eng Mech 2010;136(11):1366–79.

[37] Zhang C, Binienda WK, Goldberg RK, Kohlman LW. Meso-scale failure modeling of single layer triaxial braided composite using finite element method. Compos A Appl Sci Manuf 2014;58:36–46.

[38] Li Z, Khennane A, Hazell PJ, Brown AD. Impact behaviour of pultruded GFRP composites under low-velocity impact loading. Compos Struct 2017;168:360–71.

[39] Ramberg W, Osgood WR. Description of stress-strain curves by three parameters. 1943.

[40] Standard Australia. Metallic materials-tensile testing at ambient temperature. AS 1391-2007, Sydney: SAI Global Limited, 2007.

[41] Popovics S. A numerical approach to the complete stress-strain curve of concrete. Cem Concr Res 1973;3(5):583–99.

[42] ACI (American Concrete institute). Building code requirements for structural concrete (ACI 318-19) and commentary. ACI 318-19, Farmington Hills, MI, 2019.

[43] Standard Australia Methods of testing concrete-Determination of the compressive strength of concrete specimens AS 1012.9 2014 SAI Global Limited Sydney.

[44] Du Y, Chen Z, Wang YB, Liew JR. Ultimate resistance behavior of rectangular concrete-filled tubular beam-columns made of high-strength steel. J Constr Steel Res 2017;133:418–33.

[45] Hassanein MF, Elchalakani M, Karrech A, Patel VI, Yang Bo. Behaviour of Concrete-filled Double-skin Short Columns Under Compression Through Finite Element Modelling: SHS Outer and SHS Inner Tubes. Structures 2018;14:358–75.

[46] Lin Guan, Teng JG. Advanced stress-strain model for FRP-confined concrete in square columns. Compos B Eng 2020;197:108149.

[47] Chan C, Yu T, Zhang S. Compressive behaviour of square fibre-reinforced polymer–concrete–steel hybrid multi-tube concrete columns. Adv Struct Eng 2018; 21(8):1162–72.

[48] Shahawy M, Mirmiran A, Beitelman T. Tests and modeling of carbon-wrapped concrete columns. Compos B Eng 2000;31(6–7):471–80.